Micro-Mechanics of Fatigue Damage in Pb-Sn Solder Due to Vibration and Thermal Cycling

A. DASGUPTA,* P. SHARMA AND K. UPADHYAYULA

CALCE Electronic Products and Systems Consortium, University of Maryland, College Park, MD 20742

ABSTRACT: This paper presents a micro-mechanistic approach for modeling fatigue damage initiation due to cyclic plasticity and cyclic creep in eutectic Pb-Sn solder. The issue of damage evolution is deferred to a future paper. Fatigue damage model due to cyclic plasticity is modeled with dislocation mechanics. A conceptual framework is provided to quantify the influence of temperature on fatigue damage due to cyclic plasticity. Damage mechanics due to cyclic creep is modeled with a void nucleation model based on micro-structural stress fields. Micro-structural stress states are estimated under viscoplastic phenomena like grain boundary sliding and its blocking at second phase particles, and diffusional creep relaxation. A conceptual framework is provided to quantify the creep-fatigue damage due to thermo-mechanical cycling.

1. INTRODUCTION

EUTECTIC Pb-Sn SOLDER used in electronic packaging applications is known to be highly viscoplastic in use environments because of the high homologous temperatures. When used as interconnects in surface mount electronic circuit card assemblies (CCAs), these materials age and experience fatigue damage due to complex combinations of vibration loading and cyclic thermo-mechanical loading throughout their life cycle as well as during accelerated life tests. Quantifying the damage and relating accelerated test results to use environment are challenging tasks because of the differences in load profiles and micro-structural aging rates.

Fatigue damage due to vibration loading is primarily due to cyclic plasticity while that due to temperature cycling is primarily by cyclic creep. In this paper, "plastic" deformations refer to those occurring over almost instantaneous time

*Author to whom correspondence should be addressed.

1530-7921/01/02 0101–32 $10.00/0 DOI: 10.1106/NM1B-1UQH-DJCT-4YH1

scale due to dislocation slip; "creep" deformations refer to those occurring over longer time scales due to diffusion-assisted mechanisms such as grain boundary sliding, dislocation glide/climb and mass transport through the grain boundary or the matrix. Furthermore, there are interactions between vibration and temperature damage accumulation rates due to: (1) temperature dependent changes in material properties; (2) progressive micro-structural coarsening; and (3) rapidly alternating vibration stresses superposed on slowly varying mean stresses caused by thermo-mechanical cycling. This paper mechanistically explores fatigue damage accumulation under both conditions, and their interactions.

Currently there are several phenomenological continuum models in the literature for fatigue damage of Pb-Sn eutectic solder. The primary indicators of damage are chosen through a qualitative understanding of the underlying failure mechanisms and the model constants are obtained by empirical ewe-fits to experimental data. The underlying physical mechanisms and microstructural changes responsible for the damage are not explicitly "embedded" in these models. Examples of models which fall into these categories are: total strain range model (Coffin, 1971; Manson, 1966; Solomon et al., 1988, Logsdon et al., 1990), strain-range partitioning model (Hirschberg and Halford, 1976), cyclic energy dissipation models (Solomon, 1986; Vaynman and Fine, 1991, Darveaux et al., 1995), energy partitioning model (Dasgupta et al., 1992), continuum damage models (Ju et al., 1996; Basaran and Chandraoy, 1998; Chow et al., 1998).

While macroscopic "phenomenological" models are attractive as design tools because of the ease of implementation, they cannot be easily extrapolated to loadings or micro-structures beyond the range of available data because of their empirical nature. For more robust quantification of the damage process the underlying physical mechanisms that drive the failure process must be investigated at the micro-structural length scales. Furthermore, it is very important to base the damage model explicitly on the micro-structural state because of the need to assess acceleration factors when micro-structural evolution in short accelerated test environments is significantly different from that encountered over long time scales in the life cycle environment.

The failure process is usually partitioned for convenience into two overlapping phases: damage initiation and damage growth/propagation. Initiation and growth of distributed micro-structural damage usually alter the macro-scale effective properties, and effective homogenization techniques are needed to track the damage evolution. In this paper, the focus is on the initiation phase. Micro-mechanics issues in modeling damage evolution will be presented in a future paper.

The paper is divided into two parts. Vibration induced fatigue damage due to cyclic plasticity (and its interactions with thermal cycling) is addressed in Section 2 while cyclic creep-fatigue damage due to thermal cycling is discussed in Section 3. Micro-mechanics models available in the literature are enhanced and improved, as necessary, to be applicable to the present problem.

2. VIBRATION FATIGUE DUE TO CYCLIC PLASTIC DEFORMATION

Vibration causes high strain-rate deformations, which are caused primarily by "plastic" mechanisms. To quantify the damage caused by temperature-vibration interactions at a micro-structural level, it is necessary to consider micro-structural evolution and the dislocation motion necessary to cause cyclic "plastic" deformation. Thus the main objective in this section is to present a micro-mechanistic incremental damage superposition approach (micro-IDSA) to predict temperature-dependent changes in fatigue damage initiation due to cyclic "plastic" deformations in the tin matrix of eutectic tin-lead solder.

2.1 Review of Fatigue Crack Initiation Models

Several models have been proposed to explain the crystalline basis of "plastic" fatigue (Tanaka and Mura, 1981; Mura and Nakasone 1990; Suresh, 1998), based on the experimental observation of closely spaced, but distinct, slip planes (termed persistent slip bands—PSB) accommodating "plastic" deformation during the forward and reverse segments of cyclic loading. Further modifications have been proposed (Mura and Nakasone, 1990) to describe the fatigue crack initiation process based on the concept of Gibbs free energy change from a state of dislocation dipole accumulation to a state of crack initiation at the tip of the PSB, in the grain boundary.

These models have been applied to electronic packaging materials like eutectic Pb-Sn solder and compared with experimental results, with varying degrees of success (Guo and Fine, 1992). The assumptions and limitations of prior applications of the PSB model have been extensively discussed in the literature (Weertman, 1990; Chou and Li, 1969, Armstrong, Chou and Louat, 1966; Chou and Whitmore, 1961). The assumptions addressed in this study are: (1) The far-field stress is used in the model. In reality, the local stress field available to drive the dislocation dipole is often different from the far-field critical resolved shear stress (τ_{CRSS}); (2) micro-structural grain evolution is neglected. In cyclic loading, the grain structure does evolve as a function of the applied stress, elapsed time (or number of cycles) and is often accelerated by thermally activated diffusion mechanisms; and (3) mean stress effects on fatigue crack initiation are neglected. On a continuum scale, it has been experimentally verified that a tensile mean stress decreases the fatigue life while a compressive mean stress enhances the fatigue life, when the cyclic stress history is not fully reversed (Morrow, 1965; Suresh, 1998). The PSB model is enhanced in this paper to address these limitations. The overall step-by-step approach is depicted in Figure 1 and its various constituents are discussed in Sections 2.2–2.5.

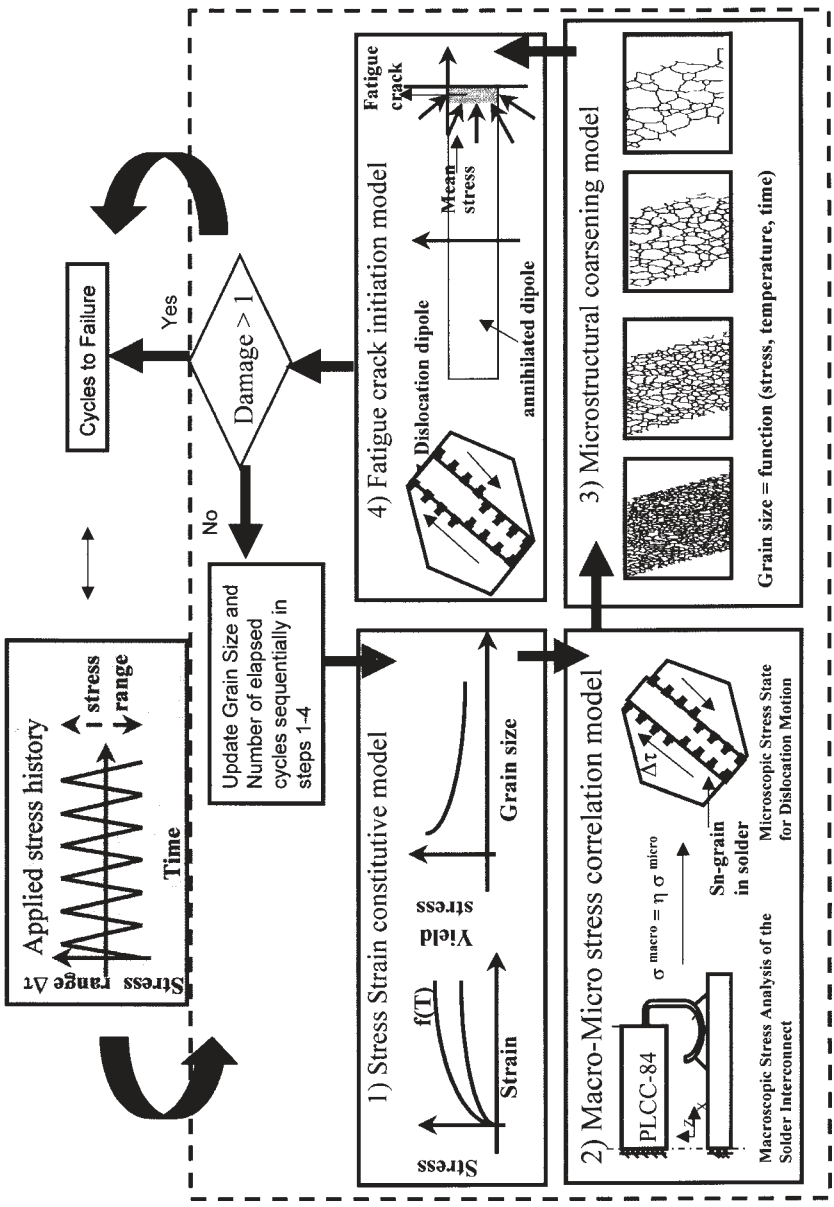

Figure 1. Micromechanistic damage model for cyclic plasticity.

2.2 Micro-Macro Stress Transformation

Local anisotropy, grain boundary sliding, grain rotation, and presence of inhomogeneities can cause high stress concentrations at grain boundaries or at triple point junctions and a corresponding decrease of stresses in the interior of individual grains. Thus the stress driving a PSB must be estimated from the far-field stresses. Macro-micro correlations for stress and strain have been derived for ductile polycrystalline and frictional materials and have been successfully applied to predict solder durability (Zubelewicz et al., 1989; 1990). An overview of the stress transformation model is presented below for completeness.

When enough slip systems are available along the principal shear direction (in other words, when damage is primarily initiated along the principal shear direction) the overall far-field macro-scale stress (σ^{ov}) is related to the average micro-scale local stress (σ) by the following expression:

$$\sigma^{ov} = \eta\sigma \tag{1}$$

where η represents the hardening-recovery damage characteristics over a representative volume. From the experimental data reported for Pb-Sn eutectic solder (Zubelewicz, 1990), η is obtained as

$$\eta = \left\lfloor 0.5 + 0.67 * N(\Delta\varepsilon_p^{ov})^{1.3} \right\rfloor \tag{2}$$

where N is the number of applied cycles and $\Delta\varepsilon_p^{ov}$ is the far-field applied plastic strain range. For simplicity of illustration, in this paper the parameter η is assumed to be a constant, with an average value of 2, based on experimental observations at the strain range of interest (Zubelewicz, 1990).

2.3 Micro-Structural Coarsening

At typical cooling rates encountered in commercial manufacturing, the microstructure of Pb-Sn solder consists of equiaxed Pb islands in a polycrystalline Sn matrix. Variations in solidification rates, and life cycle conditions can cause a wide range of microstructures and a corresponding range of constitutive and damage properties (Morris et al., 1990, 1993). Micro-structural coarsening occurs throughout the life, driven by super-plastic deformation, and has been observed to affect fatigue damage initiation. Micro-structural coarsening increases with increasing strain rate in a wide variety of two phase alloys (Arrowood et al., 1990). Several theoretical models have been proposed to model the kinetics of the grain growth. The coarsening theory of Senkov and Myshlyaev (Senkov et al., 1986) has been successfully applied by several researchers (Hacke et al., 1993, 1997; Okura,

1999). In particular, the solder microstructure has been experimentally observed to coarsen in accordance with the cubic coarsening model (Hacke, Spreche and Conrad, 1993):

$$d^3(t) - d_0^3(t) = \frac{c_1 t}{T} \exp\left(-\frac{\Delta H_g}{RT}\right) \tag{3}$$

where d is the mean phase diameter at time t, d_o is the mean phase diameter (also referred to as initial or as-cast grain size) at time $t = 0$, c_1 is a kinetic factor that depends on matrix composition (in μm^3 K/hour), ΔH_g is the activation energy for volume diffusion of atoms, R is the universal gas constant and T is the temperature in Kelvin. There is a growing consensus that the effect of mechanical stress (or strain) should be included in Equation (3) (Arrowood, 1990; Nabarro, 1998). Therefore, we propose a more generalized coarsening model as

$$d^3(t) - d_0^3(t) = \frac{c_1 t}{T} \exp\left(-\frac{\Delta H_g}{RT}\right)\left[1 + \left(\frac{\Delta\tau}{c_2}\right)^{n_c}\right] \tag{4}$$

where c_2 is a reference stress in MPa, $\Delta\tau$ is the cyclic stress range in MPa and n_c is the stress exponent. Since the primary driver for cubic coarsening model is the bulk (or volume) diffusion of atoms, a value of unity is selected for the stress exponent n_c. Also in reality, the micro-structure coarsens until a saturated (or equilibrium) configuration (or grain size) is achieved (Morris et al., 1993). Based on the commonly observed grain sizes in solder literature, a saturated grain size of 40 μm (Kashyap and Murty, 1982) is selected for illustrative purposes in this study. The model constants used in this study (presented in Table 1) are obtained from the microstructure data reported in solder literature (Hacke et al., 1993).

2.4 Fatigue Crack Initiation

In this section, the formulation of the PSB model (Mura and Nakasone, 1990) is briefly summarized for completeness, and then enhanced in Section 2.4.1 to include mean stress effects. The procedure is schematically illustrated in Figure 2. Under a cyclic shear stress ($\Delta\tau$), shown in Figure 2(A), the forward and reverse displacements are assumed to be accommodated within two closely spaced, parallel dislocation slip planes that constitute the PSB, schematically shown in Figures 2(B) and 2(C). The model postulates that in order to experience fatigue, the pair of dislocation dipole distributions formed on the slip planes (layers I and II) are separated by a distance h (dipole height). The elastic strain energy (W_1) due to the PSB is evaluated to be the sum of the self-energies (on layers I and II) due to all piled-up

Table 1(a). Microstructural coarsening model constants at 25°C.

Model Parameter	Value
Temperature (T)	25°C = 298 K
Activation energy for volume diffusion of atoms (ΔH_g)	94 KJ/mol
Universal gas constant (R)	8.314 J/mol·K
Matrix composition constant (c_1)	4.2 e+15μm^3 K/hour
Stress exponent (n_c)	1
Saturated grain size (d_{sat})	40 μm
Initial grain size (d_o) [aged for 60 hours]	8.3 μm
Reference stress (c_2)	64.52 MPa

dislocations and the interaction energy between the two layers. Due to irreversibility of the dislocation creation, there is eventually enough energy available to initiate a crack of length c, shown in Figure 2(D). The Gibbs free energy change (ΔG) in going from a state of dislocation dipole accumulation to one of crack nucleation is given by the following expression:

$$\Delta G = -(W_1 + W_2) + 2c\gamma_s \tag{5}$$

where γ_s is the surface energy density at each face of the crack faces. The stored energies W_1 and W_2 are released on crack formation and $2c\gamma_s$ is the energy needed to create the two free surfaces of the crack. Crack formation is energetically favored, when the Gibbs free energy change becomes unstable and reaches a maximum value [as shown in Figure 2(E)]:

$$\frac{d}{dn}(\Delta G) = 0 \tag{6}$$

Equation (6) tracks this instability and provides an expression to estimate the critical number of cycles (N_i) to initiate a crack in the grain boundary under completely reversed cyclic shear stresses with no hydrostatic mean stress. Without inclusion of mean stresses Equation (6) results in the following relation:

Table 1(b). PSB model inputs at 25°C.

Model Parameter	Value
Lattice resistance (τ_i)	1.4 MPa
Surface energy (γ)	0.6 N/m
Dipole height (h)	0.16 nm
Elastic modulus (E)	35811 MPa
Poisson's ratio (ν)	0.3

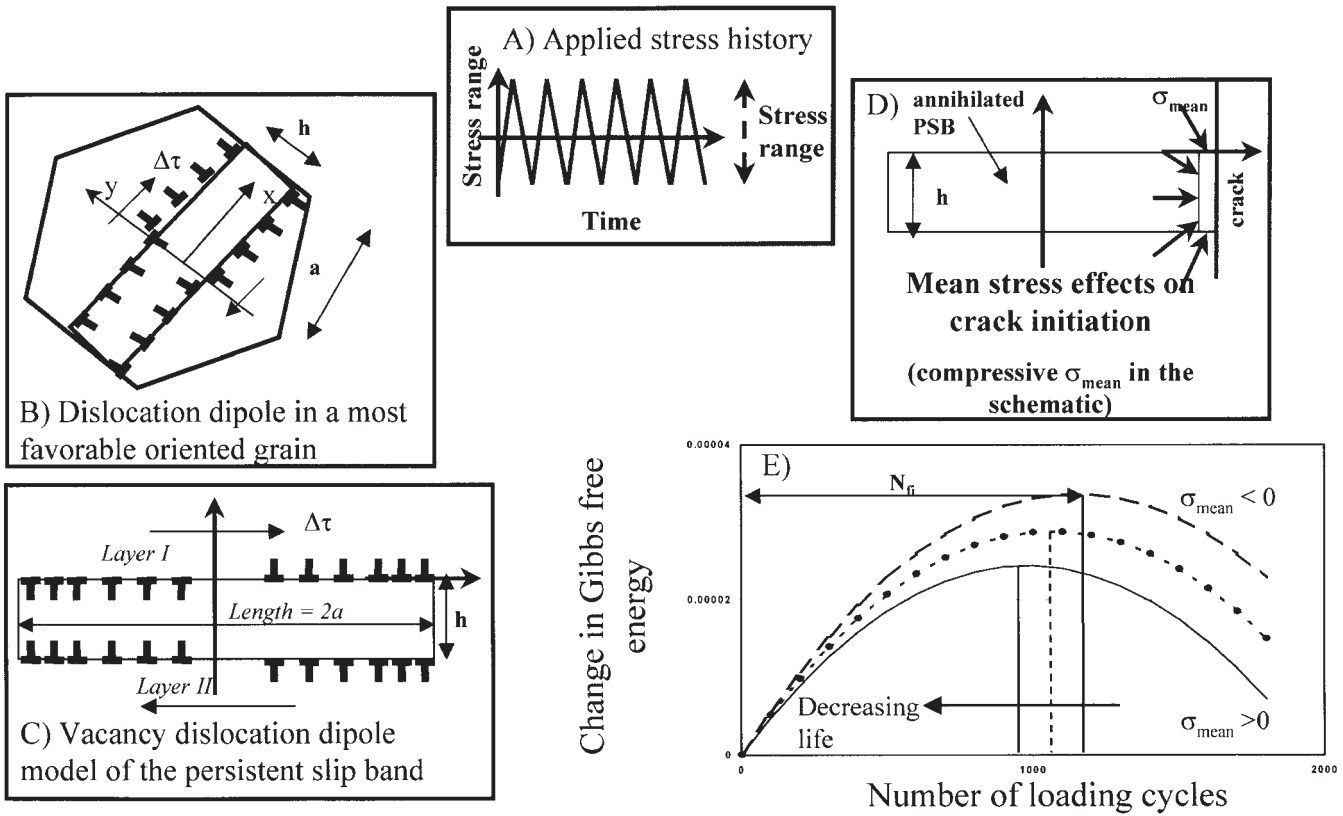

Figure 2. *Dislocation dipole model of the persistent slip band for fatigue crack initiation.*

$$\left.\begin{aligned}
&(\Delta\tau)^3 - 2\tau_f(\Delta\tau)^2 + L(\Delta\tau) - (C_1 + C_2) = 0 \\
&L = \frac{4g\varepsilon\mu^2}{\pi(1-\nu)^2}\left(\log\left(\frac{8a}{h}\right) - 1.5\right) \\
&C_1 = \frac{4\mu^2}{\pi(1-\nu)^2}\left(2g\varepsilon\tau_f\left\{\log\left(\frac{8a}{h}\right) - 1.5\right\}\right) \\
&C_2 = \frac{4\mu^2}{\pi(1-\nu)^2}\left(\frac{2-f}{fN_{fi}}\right)\left\{\frac{\gamma}{a}\right\}
\end{aligned}\right\} \tag{7}$$

where ν = Poisson's ratio; $\Delta\tau$ = applied shear stress range; τ_f = frictional stress; N_{fi} = critical number of loading cycles; $2a$ = length of slip band (~ grain diameter); h = dipole height (slip band spacing); g = fraction of elastic strain energy used in crack initiation; ε = non-dimensional parameter (= h/a); μ = shear modulus; f = irreversibility factor; γ = surface energy of each crack.

2.4.1 MEAN STRESS EFFECTS

In this paper we propose an approximate method to include the mean stress (hydrostatic stress) effects in the PSB model. As a first order approximation, we ignore (1) interactions between the dislocation stress field and the external mean stress field; and (2) constraint effects of adjoining grains. The change in energy due to the presence of the mean stresses, W_{mean}, is computed and added to the energy balance expression of Equation (5):

$$\Delta G = -(W_1 + W_2 + W_{mean}) + 2c\gamma_s \tag{8}$$

where

$$\begin{aligned}
W_{mean} &= \left(\int_0^a \sigma_{mean}\delta\varepsilon(x)h dx\right) = \sigma_{mean}ch \\
&= 2(1-\nu)(\Delta\tau - 2\tau_f)ahn\sigma_{mean}/\mu
\end{aligned} \tag{9}$$

where σ_{mean} is the mean stress acting on the initiated crack, $\delta\varepsilon(x)$ is the incremental strain in the PSB due to dislocation motion, μ is the shear modulus and $2a$ is the grain size. The mean stress energy either assists or inhibits the crack creation (and dislocation annihilation) depending on the "sign" (tensile or compressive), as shown in Figure 2(E). Substituting Equation (9) in Equation (8), a new expression

is now obtained for ΔG, and a new N_{fi} is estimated from Equations (6) and (7). With the inclusion of the mean stresses C_2 changes to

$$C_2 = \frac{4\mu^2}{\pi(1-\nu)^2}\left(\frac{2-f}{fN_{fi}}\right)\left\{\frac{\gamma}{a} + \frac{\sigma_{mean}h}{2a}\right\} \tag{10}$$

The damage accumulation ΔD during an increment of time Δt is defined as:

$$\Delta D = \Sigma \frac{n_i}{N_{fi}} \tag{11}$$

where, n_i is the actual number of cycles for a given load amplitude $\Delta\tau_I$ during that time period. The damage accumulation rate is now,

$$\dot{D} = \lim_{\Delta t \to 0} \frac{\Delta D}{\Delta t} \tag{12}$$

As the microstructure continues to evolve with increasing number of applied loading cycles, the grain size ($2a$) in Equation (9) continues to change with time, temperature and stress. The damage accumulation rate is thus continuously updated, based on the instantaneous grain size a.

In closure, the elements of the step-by-step flowchart of the approach (shown in Figure 1) are summarized below:

- *Step 1:* The initial grain size (as-cast grain size with no prior deformation) and cyclic histories of the critically resolved macroscopic shear stress and temperature are identified.
- *Step 2:* A micro-macro transition model is used to compute the microscopic stresses from the observed far-field (macroscopic) stresses or strains. This is primarily because the stress state required to drive dislocation pileups at the microstructural level is very different from the applied far-field stress state.
- *Step 3:* A micro-structural coarsening model is applied to incrementally track changes in grain size with changes in time, temperature and applied stress range.
- *Step 4:* For the micro-structural state and stress obtained from steps 2 and 3 the damage accumulated due to cyclic plastic deformation is computed using a PSB model and incremental damage superposition.

Steps (1)–(4) are sequentially repeated and the consequent changes in microstructure are updated, until the accumulated damage reaches unity. The fatigue life is equal to the number of cycles applied for accumulated damage to reach unity.

2.5 Application to Complex Load Histories

In this section, the micro-mechanistic damage model for cyclic "plasticity" is applied to a complex load history encountered in a random vibration test of a circuit card assembly (CCA). Using cycle counting algorithms, the random curvature histories measured by strain gages mounted on the CCA surface are first quantified in the form of range distribution functions (RDFs). Then using global-local finite element stress analysis of the solder interconnect, the PWB curvature RDFs are used to compute stress and strain RDFs in the solder joint. The details for estimating the stress RDFs are described elsewhere (Upadhyayula and Dasgupta, 1997). The strain and stress RDFs in the solder joint are used as inputs to the micro-scale damage model.

To demonstrate the methodology for (and to investigate the importance of) incorporating micro-structural parameters in damage models, the solder interconnect of an 84 pin J-leaded plastic IC package (PLCC-84) is subjected to a simulated isothermal aging followed by vibration loading at 90°C for 0, 1, 60 and 1000 hours. The schematic of a PLCC-84 interconnect, deformed by vibration-induced PWB curvature, is shown in Figure 3a.The PWB curvature used for this exercise is obtained from vibration at room temperature, as shown in Figure 3b (Upadhyayula and Dasgupta, 1997). Figure 3c shows the effect of micro-structural coarsening on damage predictions. The damage predictions for each case are normalized by the corresponding predictions when coarsening effects are ignored. Figure 3a demonstrates that damage predictions can vary by approximately 20% if coarsening effects are ignored. This difference will increase for vibration at elevated temperatures or when combined with temperature cycling.

The model is applied to a 60-hr combined temperature and vibration accelerated test shown in Figure 4. Details of the experiments are presented elsewhere (Upadhyayula and Dasgupta, 1997). PWB's curvature RDFs for quantifying the vibration-induced damage are obtained at the extremes and the mean of the thermal profile. The mean stresses estimated from macroscopic thermo-mechanical stress analysis (Upadhyayula and Dasgupta, 1997) are used at the microscopic level, as shown in Figure 3d. As an approximation, the total damage accumulated under combined environments is calculated for the micro-structural state obtained from 60 hours of exposure to the thermal profile of interest (shown in Figure 3d). The fatigue damage is estimated by integrating the damage accumulation rate (which depends on the instantaneous values of the micro-structural state, applied vibration loading, temperature, and thermo-mechanically generated hydrostatic stress).

Figure 4 indicates that the micro-mechanistic damage predictions provide an unexpected prediction that damage due to this combined test environment (labeled "TC + RSV") is less than the damage due to similar vibration excitation at room temperature (labeled "RSV at 25°C"). The predicted trends agree qualitatively

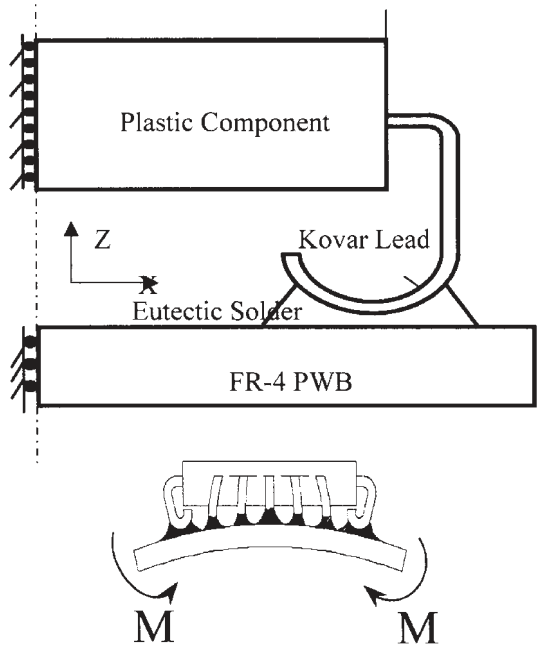

Figure 3a. *Schematic of J-leaded PLCC-84 component.*

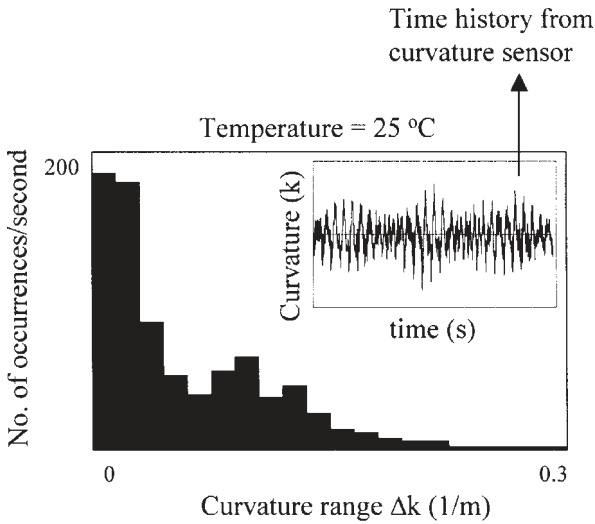

Figure 3b. *Curvature RDFs at PLCC-84 location for an input vibration excitation of 40 GRMS: from cycle counting techniques.*

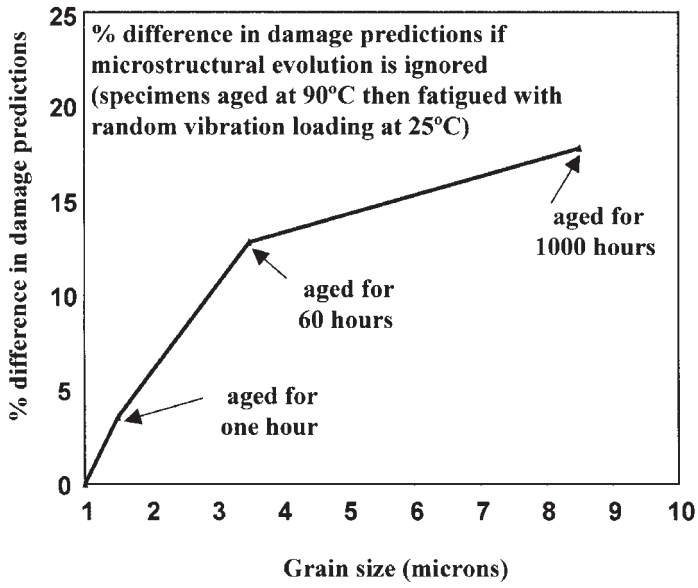

Figure 3c. *Effect of microstructural coarsening on damage predictions.*

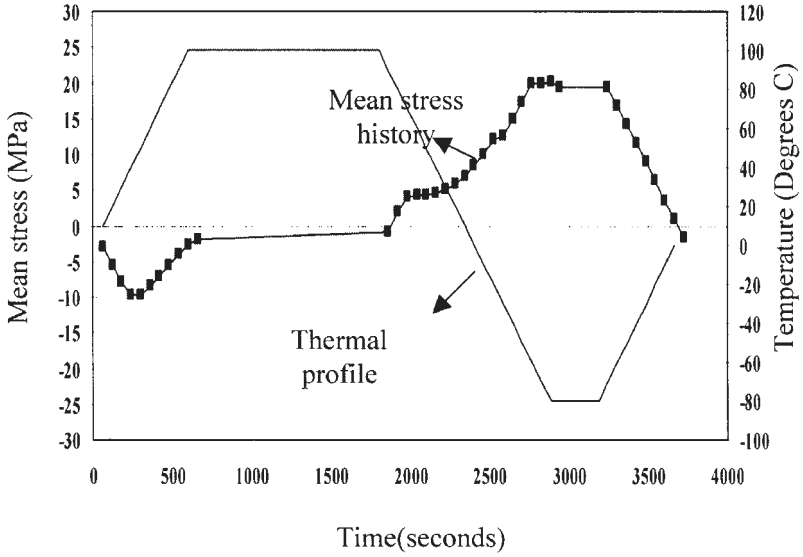

Figure 3d. *Mean stress history for PLCC-84 used in the PSB model.*

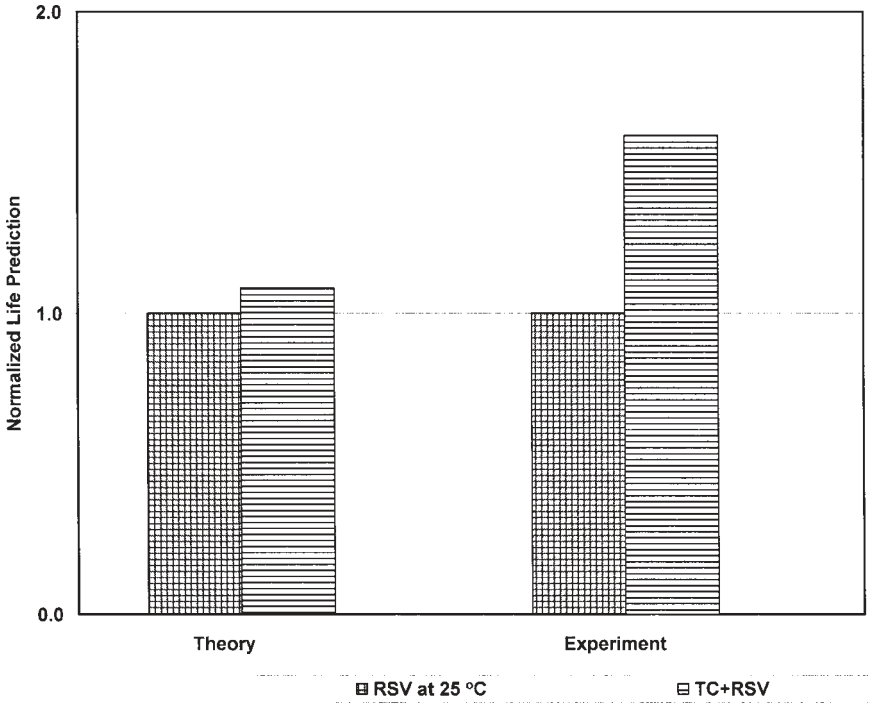

Figure 4. *Comparison of theory and experiment for PLCC-84 interconnect.*

with experimental results (Upadhyayula and Dasgupta, 1997), thus suggesting that the model captures the dominant temperature and vibration interaction effects. These results clearly indicate that a simple Miner's rule is inappropriate for such combined loading environments. As indicated before, the focus in this study is limited to an investigation of crack initiation mechanisms and therefore the contribution of crack propagation mechanisms is deferred to a future study.

3. THERMOMECHANICAL FATIGUE DUE TO CYCLIC CREEP DEFORMATION

In creep-fatigue of solder joints due to temperature cycling, several damage mechanics issues, which were not considered in Section 2, become dominant: (1) viscous grain boundary sliding (gbs); (2) blocking of gbs at second phase particles, (3) stress relaxation (4) void nucleation, growth and coalescence (Riedel, 1987). A major difficulty in modeling void nucleation is the estimation of the local stress

state because of the micro-structural viscoplastic deformation mechanisms listed above. A few researchers have proposed micro-mechanistic damage models for creep-fatigue interactions in solder. Wong and Helling's model based on void nucleation and growth (Wong and Helling, 1990) uses the far-field stresses as the driving force (i.e., local stress perturbations due to grain boundary sliding, second phase heterogeneities, and creep relaxation are not taken into account). In the micro-mechanistic model by Kuo et al. (1995), nucleation is altogether ignored and the model is not sensitive to local micro-structural deformation phenomena. A method to characterize the micro-structural stress state and its application in study of the void nucleation, void growth and cavitation instability are discussed in this section.

The physical morphology which needs to be modeled is shown in Figure 5a. As shown in the figure, grain boundaries in the matrix slide viscously at high temperatures and when impeded by second phase Pb particles, high local stress concentrations can develop at the particle-matrix interface. At high temperatures, creep mechanisms such as grain boundary, interfacial and volume diffusion, dislocation glide-climb, and void nucleation, tend to relax the high stress concentrations developed due to blocking of grain boundary sliding. The overall approach to calculate damage due to creep-fatigue mechanisms is depicted in Figure 6. In Sections 3. 1–3.3 we will mainly consider analytical means to perform micro-macro stress history transformations under creeping conditions. The impact of this transformation on void nucleation modeling is presented in Section 3.4.

3.1 Micro-Macro Stress Transformations

In Section 2.2, micro-macro stress transformations were used to estimate the local stress to drive the PSB within the grain, using a model developed by Zubelewicz et al. (l989, 1990). For the creep problem, the local stresses must be estimated at grain boundary intersections, and the problem is formulated using Eshelby's formalism of eigenstrains (Eshelby, 1957).

Consider again the configuration in Figure 5a. For simplicity of demonstration, the second phase particle (Pb phase) is modeled as a spherical inhomogeneity (see Mura (1987) for detailed definitions of inclusion, inhomogeneities and eigenstrains) situated at the end of the grain boundaries. The impinging grain boundary is modeled as a cuboidal inclusion with a prescribed stress-free eigenstrain (which is equal to the grain boundary sliding strain). The spherical inhomogeneity has radius a while the cuboidal inclusion has half-lengths a_1, a_2 and a_3. The surrounding matrix is assumed to be isotropic and elastic.

This geometric configuration is capable of modeling a wide variety of realistic microstructures. The local stresses at Point A are of primary interest because that is where the highest tensile mean stresses occur and drive void nucleation. The resulting stress field has contributions from: (1) blocking of the grain boundary slid-

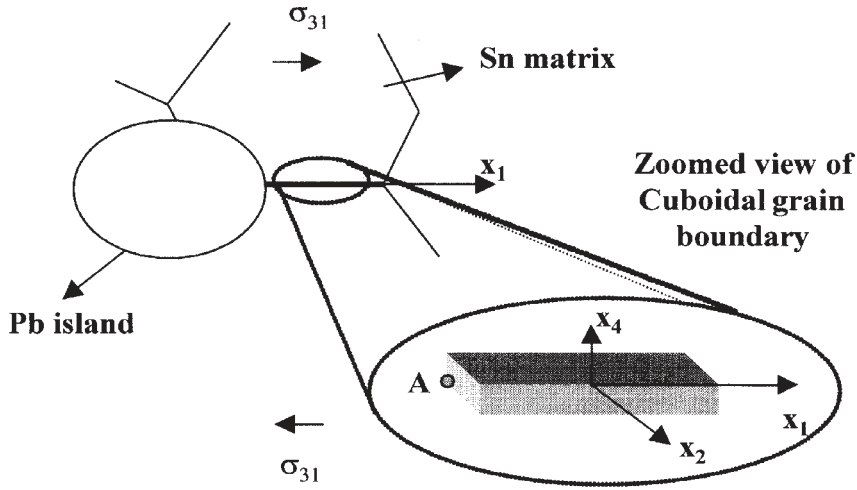

Figure 5a. *Geometric configuration.*

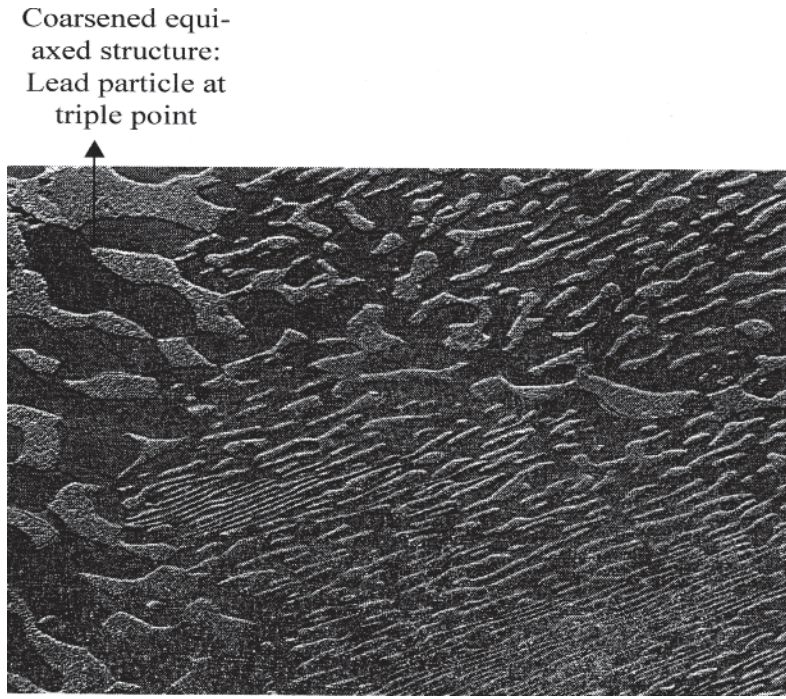

Figure 5b. *ESEM photograph of typical solder micro-structure: coarsened equi-axed structure (top-left) (Lau, 1991).*

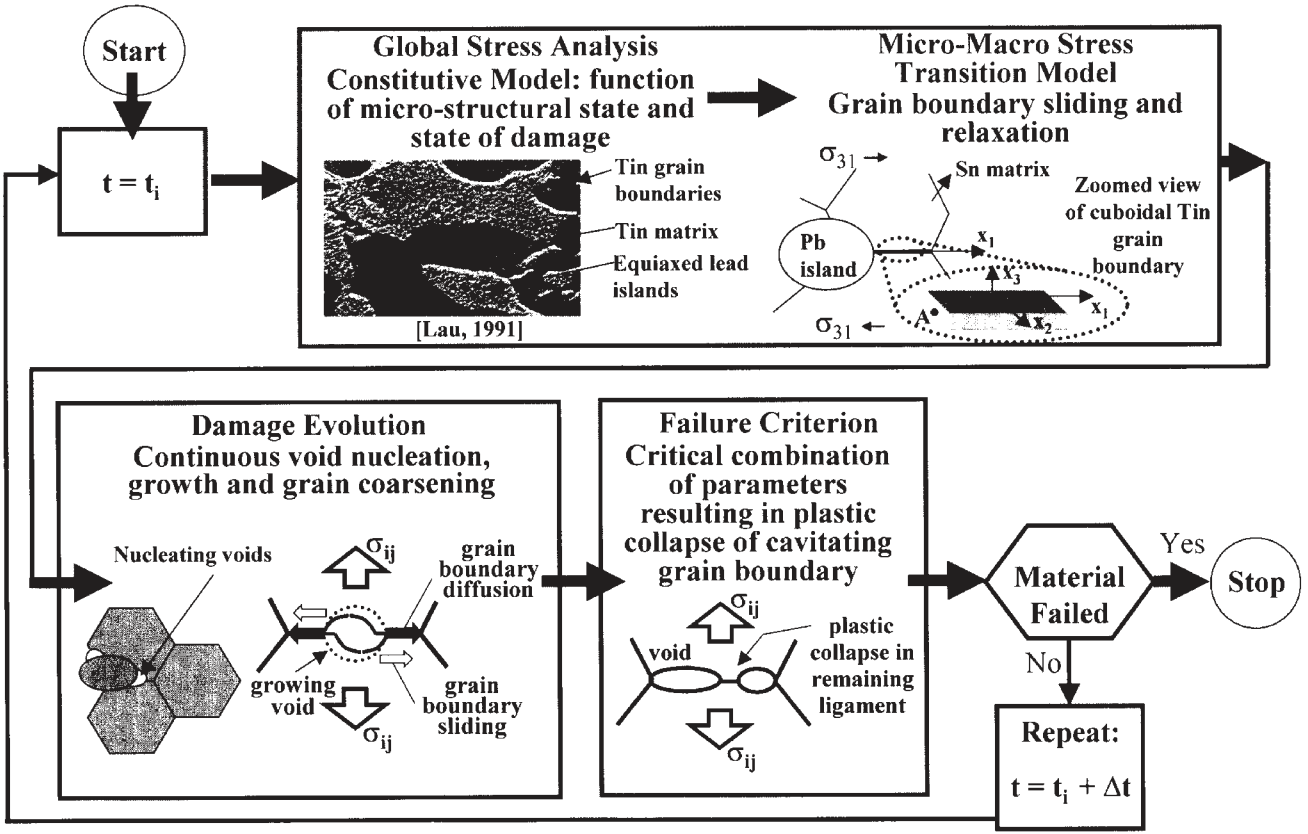

Figure 6. *Approach for damage calculation under creep-fatigue conditions.*

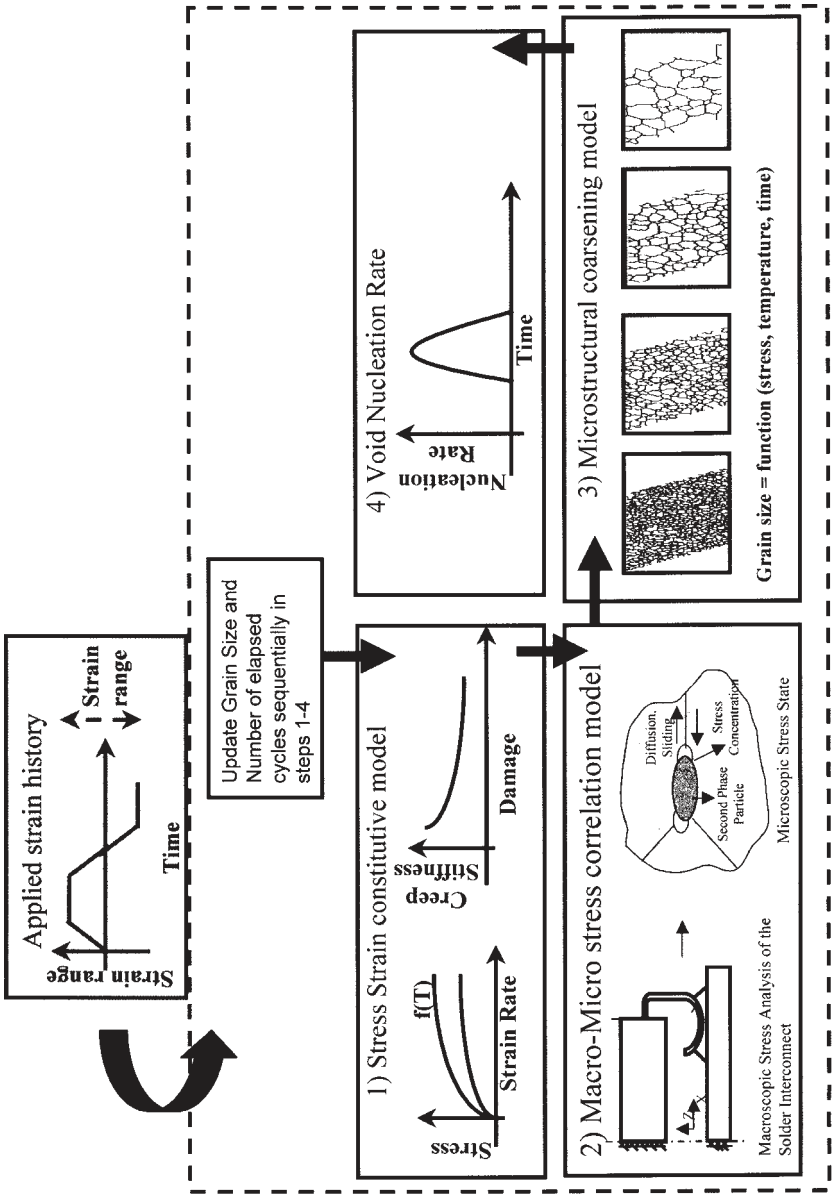

Figure 6 (continued). *Approach for damage calculation under creep-fatigue conditions.*

ing, and (2) interactions with the second phase particle. Thus Eshelby's formalism is an attractive mathematical model for these physical phenomena. Details of the model are presented elsewhere (Sharma and Dasgupta, 2000) and only the final expression is presented here to discuss the characteristics of the solution:

$$\boldsymbol{\Omega}_{\mathbf{e}} : \quad (x = A, \text{ Figure 5a})$$

$$\begin{aligned}\sigma_{ij} &= \mathbf{C}_{ijkl}(\varepsilon^{o}_{kl} + \mathbf{S}^{\mathbf{e}}_{ijkl}(\varepsilon^{*}_{kl} + \varepsilon^{R1}_{kl}) + \mathbf{D}^{\mathbf{c}}_{ijkl\_A}(\varepsilon^{gbs}_{kl} + \varepsilon^{R2}_{kl}) - \varepsilon^{*}_{kl}) \\ &= \mathbf{C}^{\mathbf{h}}_{ijkl}(\varepsilon^{o}_{kl} + \mathbf{S}^{\mathbf{e}}_{ijkl}(\varepsilon^{*}_{kl} + \varepsilon^{R1}_{kl}) + \mathbf{D}^{\mathbf{c}}_{ijkl\_A}(\varepsilon^{gbs}_{kl} + \varepsilon^{R2}_{kl}))\end{aligned} \tag{13}$$

Here, $\mathbf{S}^{\mathbf{e}}$ is Eshelby's strain concentration tensor for interior points, while $\mathbf{D}^{\mathbf{c}}$ is the strain concentration tensor for the cuboidal shape, but for exterior points, ε^{*} is the fictitious eigenstrain needed to represent the inhomogeneity. The superscript _*A* indicated that the cuboidal Eshelby's tensor is evaluated just outside the grain boundary, at Point A, as marked on Figure 6. ε^{gbs} is the grain boundary sliding eigenstrain in the cuboidal grain boundary. Due to volume and/or interfacial diffusion, shape/size of inhomogeneity or surrounding matrix may change. Let this be represented by eigenstrain ε^{R1} embedded in the spherical inhomogeneity. Similarly, for cuboidal grain boundary inclusion, we consider an eigenstrain ε^{R2}, although in this case, only interracial diffusion relaxation mechanism is considered. $\mathbf{C}$ is the fourth order elastic stiffness tensor for the matrix while $\mathbf{C}^{\mathbf{h}}$ is the fourth order elastic stiffness tensor for the inhomogeneity and ε^{o} is the applied strain. Conventional summation rules apply. $\boldsymbol{\Omega}_{\mathbf{e}}$: $(x = A)$ indicates that these equations are solved in the region of the ellipsoid at point A marked in Figure 5a. In reality, ε^{*} is non-uniform due to the interaction of grain boundary stress field and the inhomogeneity (Moshcovidis and Mura, 1975) and thus Equations (13) represent a set of six coupled singular integral equations.

As an approximation, we evaluate Equations (13) at Point A (Figure 5a) and use the resulting fictitious eigenstrain as a representative uniform estimate of the average eigenstrain field. Such an approximation has been shown to represent the mechanics well when the inhomogeneities are almost touching each other and only the interfacial stress concentration is sought (Sharma and Dasgupta, 2000). Other researchers take into account interactions between inclusions typically by expanding the non-uniform eigenstrain fields into Taylor's series (Moshcovidis and Mura, 1975; Rodin and Hwang, 1991). However, as shown by Rodin and Hwang (1991) convergence is very slow when the inclusions are almost touching each other.

3.2 Diffusional Relaxation of Micro-Scale Stresses

Mori et al. (1980) and Onaka et al. (1990) showed that when complete interfa-

cial and long-range volumetric diffusional relaxation takes place, the stress state becomes completely hydrostatic and equal to the applied stress (i.e., the inhomogeneity acts as if it was not present). The grain boundary sliding strain is a shearing strain and volume diffusion does not play a role. In the case of cuboidal inclusion with shear eigenstrain, diffusion occurs along the inclusion interface (i.e., grain boundary diffusion) until the grain boundary sliding eigenstrain disappears (i.e., the inclusion ceases to exist). Thus the final state of ε^{R1} is such that the fictitious eigenstrain to model the inhomogeneity as an equivalent inclusion is nullified (Eshelby, 1957). Since for any given eigenstrain, the resulting perturbed stress field in a cuboidal inclusion is always non-uniform (Chin, 1977; Mura, 1987), hydrostatic stress state is not possible and complete relaxation can only occur when $\varepsilon^{R2} + \varepsilon^{gbs} \to 0$ at $t \to \infty$. This discussion can be summarized as follows:

$$\varepsilon^{R1}(t \to \infty) = -\varepsilon^{*}(t \to \infty) \tag{14a}$$

$$\varepsilon^{R2}(t \to \infty) = -\varepsilon^{gbs}(t \to \infty) \tag{14b}$$

Strain due to grain boundary sliding (assuming Newtonian viscosity) can be written as (Chan et al., 1986; Riedel 1987):

$$\varepsilon_{31}^{gbs}(t) = -\varepsilon_{31}^{\max}(1 - e^{-t/t_{gbs}}) \tag{15}$$

Here t_{gbs} is the characteristic time for gain boundary sliding and is dependent on its viscosity. Based on the expression of viscosity for a reasonably flat boundary (Crossman and Ashby, 1975), an estimate for t_{gbs} is

$$t_{gbs} = \frac{dkT}{8bD_b\delta_b G}\phi \tag{16}$$

Here T is the absolute temperature, k is Boltzmann's constant, Ω represents the atomic volume, $D_b\delta_b$ represents the grain boundary diffusion coefficient, d is the grain boundary length (or $2a_3$) while G is the shear modulus of the material. ϕ is an unknown dimensionless factor that is closely related to the geometrical characteristics of the grain boundary. It can only be determined through indirect means.

The term $\varepsilon^{\max}$ is harder to determine however. Its upper bound is clearly some fraction of overall or average creep strain. The formulation in this paper will be demonstrated on Sn-Pb eutectic solder. Experiments by Lee and Stone (1994) on solder show that the contribution of grain boundary sliding to the overall strain is nearly 0.25 in the entire range of strain rates within which grain boundary sliding does occur. Further, if far-field stress is held constant, in the long-term limit, the far-field creep strain will reach rupture strains. In this dissertation, $\varepsilon^{\max}$ is chosen

to be approximately one-fourth of the rupture strain for the given temperature and stress. Since rupture strain also follows a power-law/Arrhenius relationship with respect to temperature and stress, the sliding eigenstrain is given by

$$\varepsilon^{\max} = A_{gbs}\sigma^{m} \exp\left(-\frac{\Delta H_{gbs}}{kT}\right) \tag{17}$$

Within the inhomogeneity, relaxation proceeds with a combination of volume and interfacial diffusion. First, interfacial diffusion (which is the faster of the two) will relax the shear stresses such that stress state becomes hydrostatic. Volume diffusion will ensue in such a manner as to counteract the fictitious eigenstrain until perturbations due to the inhomogeneity vanish. According to Onaka et al. (1990), the volumetric relaxation eigenstrain can be represented as

$$\varepsilon_{ij}^{R1}(t) = -\varepsilon_{ij}^{*}(1 - \varepsilon^{-t/t_v}) \tag{18}$$

Note that although both interfacial and volumetric diffusion occur, the relaxation time t_v is taken to be controlled by volume diffusion as it is orders of magnitude slower than interfacial diffusion. Onaka et al. (1990) give the expression for t_v (for a spherical inhomogeneity) as

$$t_v = \frac{kTa^2(3K^h + 4G)}{12GK^h\Omega D_v} \tag{19}$$

Here, a is the particle radius while G and K are the shear and bulk moduli. The superscript h indicates the inhomogeneity. D_v is the coefficient of volumetric diffusion of the tin matrix.

The relaxation mechanism within the cuboidal inclusion is considered to be grain boundary diffusion such that the net volume of the grain boundary does not change, i.e., diffusion occurs along the grain boundary to relieve the grain boundary sliding strain and also follows first order kinetics (Mori et al., 1980):

$$\varepsilon_{31}^{R2}(t) = -\varepsilon_{31}^{\max}(1 - e^{-t/t_{gbd}}) \tag{20}$$

The derivation of t_{gbd} (characteristic diffusional relaxation time) is based on two different methods. Mori et al. (1980) use a mechanistic method to derive an expression for interfacial relaxation time for a spherical inhomogeneity subjected to pure shear. An alternative method is also possible (Sharma and Dasgupta, 2000) based on the thermodynamic relaxation theory of Haslach (1999) which results in similar relaxation equations. The final expression for t_{gbr} can be expressed as

$$t_{gbd} = \frac{kTV_g}{G\Omega D_b \delta_b}\xi \tag{21}$$

Here, V_g is the volume of the grain boundary and Ω is the atomic volume and ξ (like ϕ) is a local dimensionless geometrical factor which can only be inferred indirectly through empirical means.

3.3 Void Nucleation, Growth and Instability

The micro-scale stresses, estimated in Section 3.2, cause void nucleation. Several mechanisms have been proposed for void nucleation. In general, void nucleation is still not fully understood and there is no consensus in the literature about the fundamental mechanisms. For the purposes of this study, a nucleation model suggested by Giessen and Tvergaard (1990), modified appropriately, is chosen. The only thing that is certain is that void nucleation is a continuous process and the rates are indeed sensitive to local micro-scale phenomena and stress state. Thus the model presented in Equation (22) is used in conjunction with the micro-macro transition model.

$$\dot{N} = F_o \frac{N_{\max} - N}{N_{\max}} \dot{\varepsilon}_c \left(\frac{\sigma_n}{\sigma}\right) \qquad \sigma_m > 0 \tag{22}$$

Here, the stress normal to the grain boundary (σ_n), and the rate of the creep strain rate (ε_c) are to be considered local to the nucleation sites. N is the number of nucleating voids, and $N_{\max}$ is the maximum number of nucleation sites available (function of microstructure). Remaining variables are model constants. This nucleation model requires that local σ_m (hydrostaticst ress) be positive for nucleation to occur.

Void growth occurs by three main mechanisms: grain boundary diffusion, power-law creep, and grain boundary sliding. Models are available in the literature for the first two mechanisms, but usually an upper bound solution is used for the mechanism of grain boundary sliding (see for example, Onck, 1998). A more realistic (mechanistic) model for grain boundary sliding induced void growth is described elsewhere by the authors (Sharma, 2000; Sharma and Dasgupta, 2000), and only the final expressions are given here.

Void growth due to grain boundary diffusion has been addressed by several researchers (e.g., Hull and Rimmer, 1959; Rice, 1980). The final expression is

$$\dot{V}_{diff} = 4\pi \frac{D_b \delta_b \Omega}{kT} \frac{\sigma_b - (1-\omega)\sigma_s}{\ln(1/\omega) - (3-\omega)(1-\omega)/2} \tag{23}$$

where σ_b is the local average of the normal stress perpendicular to the grain bound-

ary, ω is the void area fraction in the grain boundary. Similarly, void growth due to power law creep can be represented by (Budiansky et al., 1982; Tvergaard, 1984) Equation (24) which is used for low stress triaxiality ($\sigma_m/\sigma_e < 1$) while Equation (25) is used for triaxiality ratio greater than or equal to one.

$$\dot{V}_{cr} = 2\pi\dot{\varepsilon}_e R^3 h[\alpha_n + \beta_n]^n(\sigma_m / \sigma_e) \tag{24}$$

$$\dot{V}_{cr} = \mathrm{sgn}(\sigma_m)2\pi\dot{\varepsilon}_e R^3 h[\alpha_n(\sigma_m / \sigma_e) + \beta_n]^n \tag{25}$$

R is instantaneous void radius, σ_e is equivalent stress near the void, α_n and β_n are empirical constants. Other terms are as defined earlier. The stresses, and strain rates are to be considered local to the grain boundary facet though remote from the cavity. The void growth due to grain boundary sliding can be written as (Sharma, 2000; Sharma and Dasgupta, 2000):

$$V^*_{gbs} = \pi \frac{D_b \delta_b \Omega}{kT} \frac{R}{d} (SF)\varepsilon_{gbs} \tag{26}$$

Here SF is a shape factor, which depends on the instantaneous softening and creep behavior of the damaged material. Expressions for SF are presented elsewhere (Sharma, 2000; Sharma and Dasgupta, 2000). Remaining terms are as defined earlier.

Final failure is predicated on plastic instability of the remaining ligaments adjacent to the growing voids, in the grain boundary. A rigorous mechanistic failure criterion, based on the theory of cavitation instability, grain coarsening, progressive degradation of yield strength due to grain coarsening, porosity and hydrostatic stresses is presented elsewhere (Sharma, 2000; Sharma and Dasgupta, 2000), and only sample final results are presented in the next section. The resulting estimate of instability stress is a function of the damage state and is termed as the failure locus in subsequent discussion.

3.4 Applications to Complex Load Histories

Sample results of the micro-stress variation [Equations (13)] are shown in Figure 7. The results are plotted for different grain sizes. Only a far-field shear stress is applied (numerical inputs are provided in Table 2). Methods for determining some of the constants are presented elsewhere (Sharma and Dasgupta, 2000). The resulting principal normal stress at the particle-matrix interface is plotted (normalized with respect to the applied stress). As expected, stresses build up and relax with time, reverting finally to the applied stress.

The elements described in Section 3.3 can be combined to form a creep-fatigue

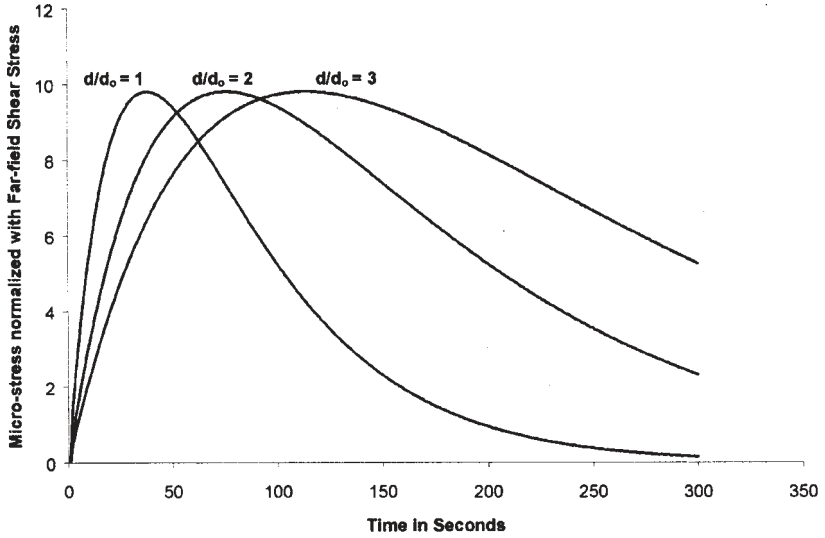

Figure 7. *Variation of normalized micro-stress with time and grain size.*

damage model. More details of such implementation are given in Sharma and Dasgupta (2000).

The effect of continuous void nucleation is taken into account by linking nucleation rate to inter-void half-spacing (λ). It can be easily shown that (Onck, 1998):

$$\lambda = \lambda \frac{N_o}{N} \tag{27}$$

where the subscript o indicates initial values.

To illustrate the micro-scale cyclic creep damage model, based on micro-scale mechanics, a simple but representative case is chosen. The configuration, as shown in Figure 8, consists of a thin layer of solder on a very thick substrate.

The substrate is assigned a higher CTE than solder and thus during a thermal cycle tensile axial stresses will develop in solder during heating and compress during cooling due to thermal expansion mismatch. The resulting stresses are assumed to be uniformly distributed. In reality, void linkage will occur at different points at different times leading to evolution of a crack. Such an analysis requires use of an advanced numerical tool like the finite element method. For now, since stresses are assumed to be distributed uniformly, we employ the concept of statistical homogeneity to analyze only a unit cell with a given grain configuration. The grain boundary or the unit cell is assumed to be oriented at an angle of 45° with respect to the direction of uni-axial macro-stress. Once failure or void interlinkage occurs in

Table 2(a). Numerical parameters.

$D_b\delta_b$ (Kuo, 1994)	7.35×10^{-15} exp(–9452/(1.987T)) m^3/s
Ω	3×10^{-30} m^3
Point of stress calculation	$10^{-8}a_1$ away from corner A in the direction of x_1
Nominal grain size	3.5 μm
Particle size	3.5 μm
A_{gbs} (approximate estimation from Frost et al., 1988)	5.11
m (approximate estimation from Frost et al., 1988)	0.182
ΔH_{gbs} (approximate estimation from Frost et al., 1988)	0.12
K (Boltzmann's constant)	1.38×10^{-23} J/K
E (elastic modulus of eutectic solder) (Okura, 2000)	25000 MPa
ν (Poisson's ratio)	0.4
E_h (elastic modulus of lead) (Okura, 2000)	12500 MPa
Applied shear stress	10 MPa
ϕ	1.0634×10^7
ξ	6.44×10^1

Table 2(b). Numerical parameters.

A	0.2557 $(MPa)^{-n}/s$
n	6.28
ΔH	0.7036
k	8.17×10^{-5}
ΔH_g (grain coarsening)	94 KJ/mol
c_1	4.2×10^{15} μm^3 K/hour
c_2	64.52 MPa
Hall-Petch relationship	(4.08 – 0.008T)/sqrt(d) + (74.326 – 0.144T) T = temperature in K, d = grain size in μm

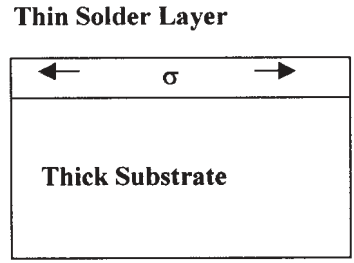

Figure 8. *Global structure.*

this unit cell, a grain-sized crack is formed. Since the damage is assumed to be uniform, failure in our entire structure will occur at nearly the same time as failure of the unit cell.

The "nominal" loading profile is defined in Table 3. The nominal case has a triaxiality ratio of nearly 0 (actually, it has triaxiality ratio of +0.333 during heating and –0.333 during cooling but since the time spent in the compressive and tensile regimes is not too different we can assume an average triaxiality ratio of 0).

For this simplified and idealized structure the global stresses can be found by solving the following differential equation:

$$\Delta\alpha \frac{dT}{dt} = \frac{1}{E}\frac{d\sigma}{dt} + A\sigma|\sigma|^{n-1} \exp\left(-\frac{\Delta H}{kT}\right) \tag{28}$$

$\Delta\alpha$ represents the difference in the CTE (Coefficient of Thermal Expansion) of the substrate and solder. ΔH is the activation energy for creep, k is Boltzmann's constant while σ is the axial stress developed in solder.

First, the void radius fraction (R/λ) plot is shown for the nominal case in Figure 9, to illustrate how damage progresses with temperature. As one would expect, the

Table 3. Nominal parameters and temperature load profile.

Temperature Range	145°C
Upper Temperature	90°C
Ramp Up Rate	10°C/min
Ramp Down Rate	10°C/min
Upper Dwell Time	10 min
Lower Dwell Time	5 min
CTE of Substrate	70 ppm/°C
Thickness of Substrate	very thick
External Hydrostatic Stress	0
Grain Size	3.5 μm

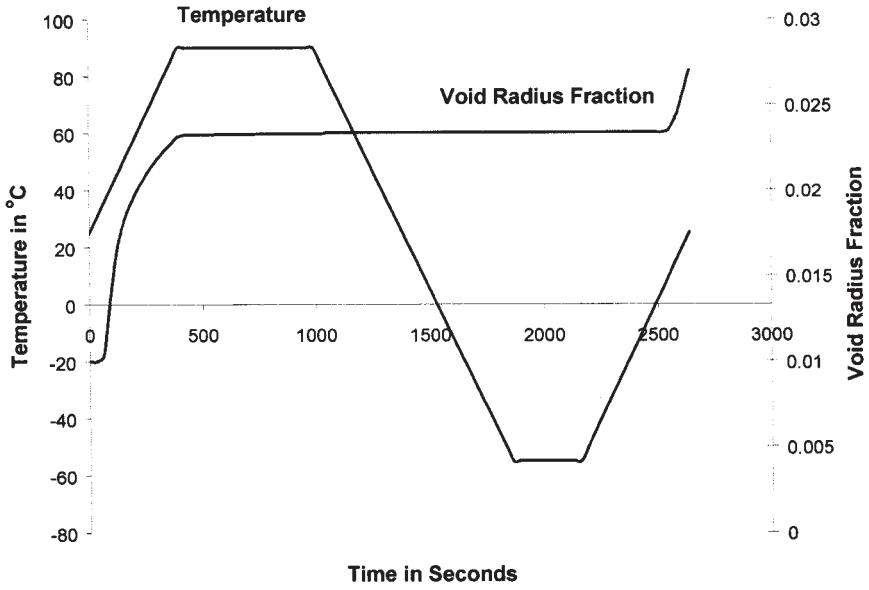

Figure 9. *Void radius fraction evolution in the first cycle.*

damage rises slowly during the initial portion of the ramp (as the temperature is not too high and stresses have not built up too much). During the latter part of the ramp, damage rises rapidly although slows down a bit towards the end of the dwell (due to stress relaxation). However, very little damage healing is observed at the lower dwell and the final ramp up to room temperature. This is so in spite of compressive stresses. The reason for this is because void healing or sintering follows the same mechanism as growth but during the compressive part of the thermal cycle temperatures are too low for any of the void healing mechanisms to be significantly active (i.e., power law creep or diffusion). It is also interesting to observe how the failure locus varies in the first cycle. Complete cyclic simulation to failure proves to be much more interesting and is discussed next.

The complete failure simulation is shown for the nominal load case. Figure 10 shows evolution of void radius fraction and failure locus until complete failure. Only the minimum points on the failure locus are plotted for clarity (otherwise a dense band appears due to the oscillations in each cycle). The dotted line indicates that at the point when the void radius fraction reaches the critical instability value, the void grows unstably and coalesces (i.e., void radius fraction instantaneously becomes one).

Note that the failure locus decreases gradually as the material degrades. Failure occurs around void radius fraction of 0.7 approximately. This is interesting, as metallographic evidence indicates 0.7 to be the general damage state at failure of

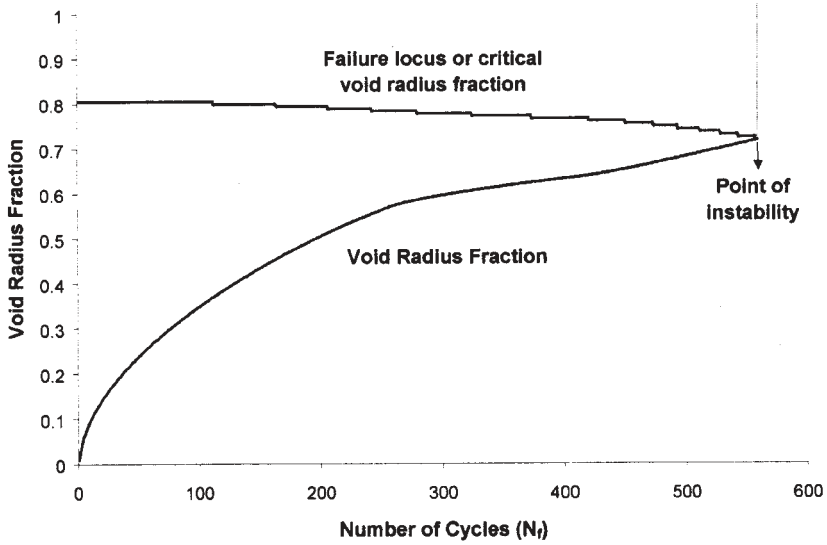

Figure 10. *Void radial and failure locus evolution until complete failure.*

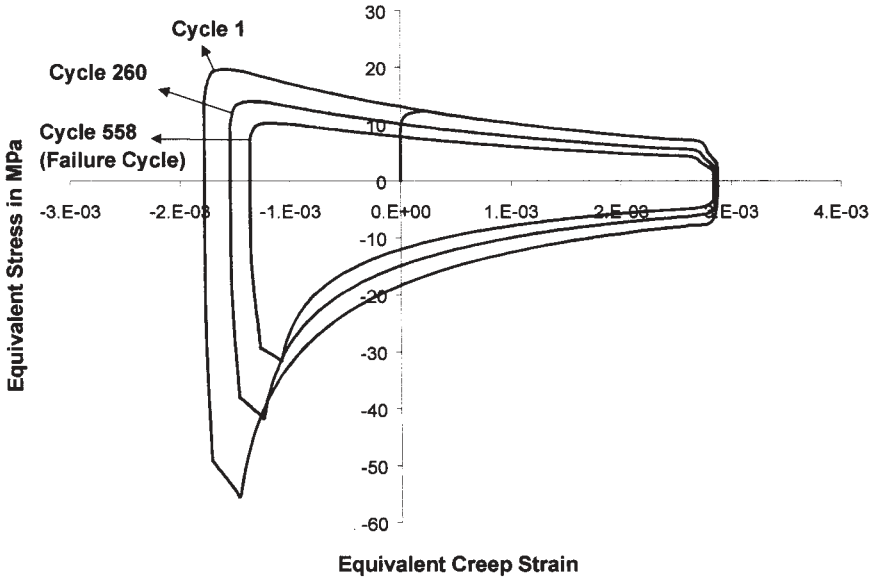

Figure 11. *Progression of cyclic hysteresis loop with damage.*

several creeping alloys. Only the minimum points on the failure locus and void radius fraction curve are plotted for clarity (otherwise a dense band appears due to the oscillations per cycle).

The constitutive properties also change as the material becomes damaged. For example, due to the drop in elastic modulus and increase in creep compliance, the collapsing hysteresis loop is shown in Figure 11. Only three hysteresis loops are shown: the initial loop, an intermediate loop and the hysteresis loop in the failure cycle (on the verge of void coalescence). The collapsing hysteresis loop can be interpreted as a progressive decrease in the material's capability to dissipate creep work and carry loads, with progressive damage. Eventually, at the point of cavitation instability, the hysteresis loop collapses completely for the unit cell being modeled.

4. CONCLUSIONS

A micro-mechanistic approach has been presented for assessing damage due to cyclic loading in viscoplastic materials such as eutectic Pb-Sn solder used in electronic assemblies. Cyclic loading occurs throughout the life cycle due to vibration and thermal cycling.

The micro-mechanistic incremental damage model for vibration fatigue damage due to cyclic "plastic" deformations includes a micro-macro stress transition model, a microstructure evolution model, a fatigue crack initiation model based on dislocation dipole pileups, which is sensitive to mean stress, and a cumulative damage metric to predict the fatigue damage due to cyclic plasticity. The details of the approach were presented in Section 2. The method was applied to complex load histories encountered in accelerated testing and the damage predictions were compared with experimental results. An important conclusion from both theory and experiments is that some combinations of thermal cycling and vibration can be less damaging than similar vibration excitation at room temperature. By incorporating the influences of microstructure in the damage predictions, this paper has provided a new modeling methodology to improve the accuracy of acceleration factor estimates across vastly different microstructures encountered in accelerated test environments and in life cycle environments. The focus in Section 2 was limited to understanding of fatigue crack initiation mechanisms and contribution of crack propagation mechanisms is not considered.

In the case of creep-fatigue of solder due to temperature cycling, some of the important physical phenomena responsible for creep damage have been analytically characterized. The blocking of grain boundary sliding by a second phase particle is modeled by an eigenstrain in a cuboidal inclusion. The effect of second phase particle inhomogeneity is also modeled approximately. The stress concentrations are a strong function of grain boundary sliding and diffusional rates. The micro-scale stresses are used to predict void nucleation rates and void growth. The resulting

degradation of material constitutive properties is modeled with homogenization theories, and the microstructural coarsening effects are also included. Eventual failure is modeled as a cavitation instability. The elements comprising various facets of cyclic creep damage were systematically combined to form a complete cyclic creep damage model.

ACKNOWLEDGEMENTS

The research for this article was performed at the CALCE Electronic Product and Systems Center of the University of Maryland. Helpful suggestions from P. R. Onck are gratefully acknowledged.

REFERENCES

Armstrong, R. W., Chou, Y. T., Fisher, R. M. and Louat, N., 1966, *Philosophical Magazine,* vol. 14, pp. 943–951.

Arrowood, R., Mukherjee, A. and Jones, W., 1990, Chapter 3 in *Solder Mechanics: A State of the Art Assessment,* Eds. Frear, D., Jones, W. B. and Kinsman, K., TMS.

Basaran, C. and Chandaroy , R., 1998, *ASME Trans. Journal of Electronic Packaging,* Sept.

Basaran, C., Desai, C. S. and Kundu, T., 1997, *ASME Journal of Electronic Packaging,* Dec.

Basaran, C. and Yan, C., (1998), *10th Symposium on Mechanics of Surface Mount Assembly—II,* ASME, Anaheim, CA.

Budiansky, B., Hutchinson, J. W. and Slutsky, S., 1982, in H. G Hopkins, M. J Sewell (eds.): *Mechanics of Solids. The Rodney Hill 60th Anniversary Volume,* Pergamon Press, Oxford.

Chan, K. S., Page, R. A. and Lankford, J., 1986, *Acta Metall.,* 34, 2361–2370.

Chiu, Y. P. (1977). *J. of Appl. Mech.,* 44, 587–590.

Chou, Y. T. and Li, J. M., 1969, Chapter in *Mathematical Theory of Dislocations,* ed. Mura, T., ASME, pp. 116–177.

Chou, Y. T. and Whitmore, R. W., 1961, *Journal of Applied Physics,* vol. 32, pp. 1920–1926.

Chow, C. I., Yang, F. and Fang, H., 1998, *ASME Winter Annual Meeting,* Nov.

Crossman, F. W. and Ashby, M. F., 1975, *Acta Metall.,* 23, 425–440.

Eshelby, J. D., 1957, *Proc. Royal. Soc.,* A241, 376–396.

Eshelby, J. D., 1959, *Proc. Royal. Soc.,* A252, 561–569.

Guo, Q., Cutiongco, E. C., Keer, L. M. and Fine, M., 1992, *Journal of Electronic Packaging,* 114, pp. 145–151.

Giessen, E. V. D. and Tvergaard, V., 1990, *Creep and Fracture of Engineering Materials and Structures,* Eds. Wilshire, B. and Evans, R.W., Elsevier, Swansea, 169–178.

Hacke, P. L., Sprecher, A. F. and Conrad, H., 1993, *ASME Journal of Electronic Packaging,* 115, pp. 153–164.

Hacke, P. L., Sprecher, A. F. and Conrad, H., 1997, *Journal of Electronic Materials,* 26, pp. 774–782.

Haslach, H. W., Jr. and Zeng, N., 1999, *International Journal of Non-Linear Mechanics,* vol. 34, no. 2 pp. 361–385.

Hull, D. and Rimmer, D. E., 1959, *Philosophical Magazine,* 4, pp. 673–687.

Ju, S. H., Sandor, B. I. and Plesha, M. E., 1996, *Transactions of the ASME. Journal of Electronic Packaging,* 118(4), pp. 193–200.

Kashyap, B. P. and Murty, G. S., 1982, *Metallurgical Transactions,* 13A, pp. 53–59.

Kuo, C. G., Sastry, S. M. L. and Jerina, K. L., 1995, *Metallurgical and Materials Transactions A,* 26A, pp. 3625–3275.

Lau, J. H. (ed.), 1991, "Solder Joint Reliability," Van Nostrand Reinhold, New York, 1991.

Lee, S. M. and Stone, D. S., 1994, *Scripta Metallurgica et Materiala,* 30, 1213–1218.

Logsdon, W. A., Liaw, P. K. and Burke, M. A., 1990, *Engineering Fracture Mechanics,* 36, pp. l83–218.

Miner, M. A., 1945, *Journal of Applied Physics,* A-159, September.

Mori, T., Okabe, M. and Mura, T., 1980, *Acta Metall.,* 28, 319–325.

Morrow, J. D., 1965, *Internal Friction, Damping and Cyclic Plasticity,* ASTM-STP 378, Warrendale, PA., pp. 45–87.

Morris, J. W. Jr. and Mei, Z., 1990, Chapter 6, in *Solder Mechanics: A State of the Art Assessment,* Eds. Frear, D., Jones, W. B., and Kinsman, K., TMS.

Morris, J. W. Jr., Goldstein, J. L. F. and Mei, Z., 1993, Chapter 2, in *The Mechanics of Solder Alloy Interconnects,* Eds. Burchett, S., Frear, D., Morgan, H., and Lau, J., Van Nostrand Reinhold, New York.

Moshcovidis, Z. A. and Mura, T., 1975, *J. of Appl. Mech.* 42, 847–852.

Mura, T. and Nakasone, Y., 1990, *Journal of Applied Mechanics,* 57.

Mura, T., 1987, *Micromechanics of Defects in Solids,* Martinus Nijhoff, Hague, Netherlands.

Nabarro, F. R. N., 1998, *Scripta Materialia,* 39, pp. 1681–1683.

Okura, J. H. and Dasgupta A., 1999, *Interpack99, ASME,* EEP 26-2, pp. 1921–1928.

Onaka, S., Miura, S. and Kato, M., 1990, *Mechanics of Materials,* 8, 285–292.

Onaka, S. and Kato, M., 1991, *Materials Science and Engineering,* A146, 217–232.

Onck, P. R., 1998, *High Temperature Fracture of Polycrystalline Materials,* PhD Thesis, Technical University Delft, Netherlands.

Palmgren, A., 1924, *VDI Zeitschrift,* No. 14, pp 339–441.

Raj, R. and Ashby, M. F., 1971, *Metallurgical Transactions,* 2, 1113–1127.

Raj, R. and Ashby, M. F., 1975, *Acta Metall.,* 23, 653–666.

Riedel, H., 1984, *Acta Metall.,* 34, 2361–2370.

Riedel, H., 1987, *Fracture at High Temperature,* Springer-Verlag, Heidelberg, Germany.

Rice, J. R., 1980, Three Dimensional Constitutive Relations and Ductile Fracture, *Proceedings of the IUTAM Symposium,* Ed. Nemat-Nasser, pp. 173–184.

Rodin, G. J. and Hwang, Y. L., 1991, *Int. J. Solids Structures,* 27, 145–159.

Senkov, O. N. and Myshlyaev, M. M., 1986, *Acta Metallurgica,* 34, pp. 97–106.

Sharma, P., 2000, Ph.D. Dissertation, Dept. of Mechanical Engineering, University of Maryland, College Park.

Sharma, P. and Dasgupta, A., 2000a, Part I to be published.

Sharma, P. and Dasgupta, A., 2000b, Part II to be published.

Suresh, S., 1998, *Fatigue of Materials,* Cambridge University.

Tanaka, K. and Mura, T., 1981, *Journal of Applied Mechanics,* 48, pp. 97–102.

Tvergaard, V., 1984, *Journal of Mechanics of Physics of Solids,* Vol. 32, pp. 373–393.

Tvergaard, V., 1991, *ZAMM. Z. angew. Math. Mech.,* 70, pp. 23–31.

Upadhyayula, K. and Dasgupta, A., 1997, *9th Symposium on Mechanics of Surface Mount Assembly,* pp. 110–117, Dallas.

Vaynman, S. and Fine, M. E., 1991, Chapter 11, *Solder Joint Reliability: Theory and Application,* Ed. Lau, J., Van Nostrand Reinhold.

Weertman, J. R., 1990, *Microstructure and Micromechanisms,* Ed. S. V. Nair, ASM Publications, pp. 335–362.

Wong, B. and Helling D. E., 1990, *Journal of Electronic Packaging,* 112, pp. 104–109.

Zubelewicz, A., Berriche, R., Keer, L. M. and Fine, M., 1989, *ASME Journal of Electronic Packaging,* 111, pp. 179–182.

Zubelewicz, A., Guo, Q., Cutiongco, E., Fine, M. and Keer, L. M., 1990, *ASME Journal of Electronic Packaging,* 112, pp. 179–182.